Exploratory Studies of the Photoproduced $\pi^0\eta$ Channel and Determination of Preliminary Cross Sections

An undergraduate thesis presented

by

Anna Woodard

to

The Department of Physics

in partial fulfillment of the requirements

for receiving

Honors in the Major

Florida State University

Tallahassee, Florida

July 2008

Thesis advisor
Volker Crede

Author
Anna Woodard

Abstract

The Crystal Barrel detector is an ideal instrument to study multi-photon final states due to its large solid angle coverage and excellent photon detection efficiency. In this study, preliminary differential cross sections of the reaction $\gamma\mathrm{p} \rightarrow \Delta\eta \rightarrow \mathrm{p}\pi^0\eta$ were extracted from data taken while the Crystal Barrel was configured with the TAPS calorimeter positioned in the forward direction. Approximately 186,000 $\mathrm{p}\pi^0\eta$ events were identified.

Trigger efficiencies and energy thresholds in the TAPS calorimeter were studied. Events were reconstructed using a missing proton kinematic fit and the $\mathrm{p}\pi^0\eta$ final state was selected via a series of confidence level cuts. $\mathrm{p}\pi^0\eta$ events were classified according to incoming photon energy E_γ and scattering angle θ^η_{cm} of the η meson in the center-of-mass system. Invariant mass spectra for the $\mathrm{p}\pi^0$ combinations (E_γ, $\cos\theta^\eta_{cm}$) were plotted.

Existing Monte Carlo (MC) software was used to simulate the experimental set-up and generate the expected mass spectra, corrected for phasespace and relativistic effects, for major contributing channels. A ROOT C interpreter script was written to determine the Δ reaction yields as a function of the incoming photon energy and scattering angle. This was accomplished by using the ROOFIT modeling toolkit to generate probability density functions (PDFs) from the MC. The $\mathrm{p}\pi^0$ spectra were then fitted with a sum of MC PDFs for the two largest isobar contributions, $\Delta^+(1232)\pi$ and $\mathrm{N}(1535)S_{11}\eta$.

The $\mathrm{p}\pi^0$ spectra indicate dominant Δ production in the threshold region. At higher energies the S_{11} contribution increases; the development of a second peak besides the Δ becomes visible around 1550 MeV. Above 1800 MeV, S_{11} production is comparable in intensity to the Δ. An unambiguous angular dependence for the S_{11} is observed over the full E_γ range as production drops off rapidly at forward angles. The fit procedure is more accurate at higher energies, where Δ and S_{11} production are well separated, and two clear peaks exist. It is likely that at lower energies the background under the Δ peak was underestimated.

Preliminary differential cross sections for $\gamma\mathrm{p} \rightarrow \Delta\eta \rightarrow \mathrm{p}\pi^0\eta$ were calculated from the Δ yields and are presented here along with an interpretation of major features. First results for the total $\gamma\mathrm{p} \rightarrow \mathrm{p}\pi^0\eta$ and $\gamma\mathrm{p} \rightarrow p\pi^0\pi^0$ cross sections are included. Agreement with previous studies is fair. Possible explanations for discrepancies are discussed.

Contents

Chapter 1

Introduction

Brief historical context of proton structure

The first evidence [1] that the proton has internal structure was the measurement of its magnetic moment by Frisch and Stern in 1933, using the diffraction of a beam of molecular hydrogen; their measured value of 2-3 magnetons was more than twice that predicted by the Dirac equation. Even more striking was the measurement of the magnetic dipole moment of the neutron by Alvarez and Bloch in 1939 [2]; if the neutron were a point particle this quantity would clearly be zero.

The first measurement of the size of the proton was performed by Robert Hofstadter in the 1950's. Although his apparatus was limited to a single massive detector on a rotating mount, using elastic electron-proton scattering at energies up to 550 MeV, he found that scattering at high energies and angles differed by a factor of nine from that expected for a point source, and calculated a radius for the proton of about $7 \cdot 10^{-16}$ m [3]. Hofstadter was awarded the Nobel Prize in 1961 for his work on nuclear and proton structure, but he considered the invention of the NaI-Tl detector to be his greatest contribution to science.

Elastic electron scattering did not, however, provide information on the proton's internal structure. In elastic scattering, kinetic energy is conserved and the energy of the scattered electron depends only on the scattering angle. However, at higher energies the scattering is inelastic; some of the energy of the incident particle is consumed in exciting the proton's internal constituents and escapes in the form of decay products. When the electron is deflected through a large scattering angle, resulting in a large momentum transfer, the process is called deep inelastic scattering. Early deep inelastic scattering experiments showed a cross-section that varied very little with momentum, suggesting that at high energies the proton behaved as a collection of constituent particles.

Clues to the properties of these constituents were provided by the dozens of new "fundamental" particles discovered by the 1960's, which were gradually organized into symmetry groups. Murray Gell-Mann and George Zweig proposed in 1963 that the structure of these groups could be explained by the existence of particles with fractional charge – the quarks.

However, free quarks could not be detected, even with the highest energy sources then available, such as cosmic rays. It was difficult to explain how the quarks could be free to interact as individual particles within the proton and yet be so strongly bound they could apparently never escape. Consequently, quarks were widely felt to be a mathematical abstraction and there were multiple competing theories of nucleon structure; the prevailing view was still that the mass and charge of the proton were "soft", or distributed [4].

Friedman, Kendall and Taylor attacked the problem in 1967, again using electron-proton scattering, but armed with still higher beam energies up to 21 GeV made available by the Stanford Linear Accelerator Center (SLAC). In his Nobel lecture, Friedman says, "For completeness, we wanted to look at the inelastic continuum since this was a new energy region which had not been previously explored. ... When the experiment was planned, there was no clear theoretical picture of what to expect [4]."

The SLAC experiments showed that at high energies the decrease in cross-section with increasing momentum was much slower than was predicted for an extended, diffuse particle, and demonstrated a scaling behavior. Bjorken had provided an analysis which demonstrated that at high energies, the form factors would depend only on the scaling variable $x = \frac{Q^2}{2pq}$ [1]; although this wasn't immediately appreciated, it gave strong evidence that nucleons contained point-like particles called partons which were later associated with quarks.

The theory of quarks still faced the fundamental difficulty that "no matter how hard hadrons were smashed into one another, one had not been able to liberate these hypothetical constituents [4]." In 1973 Gross, Politzer, and Wilczek developed an explanation for the ability of quarks to "rattle around in the proton without interacting much [5]," yet be bound so strongly that they could not exist unbound. They were awarded the 2004 Nobel Prize "for the discovery of asymptotic freedom in the theory of the strong interaction." The separation of quarks over larger distances, on the other hand, while energetically possible, produces a potential so high that a quark-antiquark pair is created, with one member binding to each of the separate quarks. It is therefore not possible to observe a free quark, an effect which is called confinement. Though confinement is not yet analytically proven, the theory of strong interactions, today known as Quantum Chromodynamics or QCD, is widely accepted.

Particles that consist of quarks (and interact strongly) are called hadrons, those comprising three quarks are called baryons. The proton consists of two up quarks and one down quark, the neutron of one up and two down quarks, for instance. The second group of hadrons, the mesons, consist of one quark and one antiquark and are all unstable, which means they decay.

1.1 Motivation for this work

A huge body of experimental evidence for QCD has been gathered over the years. Unfortunately, our understanding of the internal structure of the proton remains incomplete because the QCD Lagrangian has not been solved in the low energy regime or for bound states. Theorists have instead developed various models in an effort to arrive at a satisfactory description of hadron properties, the most successful of which are based on three constituent quark degrees of freedom. These phenomenological models are predicated on the assumption that hadrons consist of quarks with an effective mass (baryons: qqq and mesons: $\bar{\mathrm{q}}\mathrm{q}$). While a common feature in all these models is a long-range linear *confinement* potential, they differ mainly in their treatment of the residual shortrange interaction among hadron constituents.

While results from constituent quark model calculations have been reasonably successful in describing the lower part of the mass spectra, including the ground and first excited states,

[1] The dimensionless Bjorken variable x is a measure of the inelasticity, where Q^2 denotes the momentum transfer in the process.

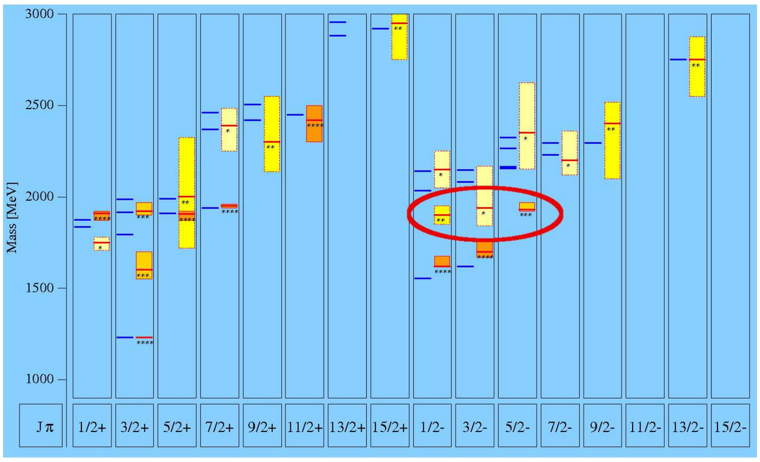

Figure 1.1: Spectrum of Δ^* baryon resonances (isospin $\frac{3}{2}$, in contrast to nucleons with isospin $\frac{1}{2}$). Left of each column: predicted masses [6]. Right: experimental values. The boxes indicate the wide range of mass measurements. The star assignments by the Particle Data Group mean that **** and *** resonances are well established, whereas * and ** resonances are not well established [8].

major discrepancies remain with regard to the treatment of higher excited states (Fig. 1.1). In the case of baryons, models predict a number of states that have not been observed experimentally. A major objective of the CB-ELSA/TAPS collaboration is to search for these undetected resonances.

The majority of observed baryon resonances has been investigated using πN scattering experiments. If some missing states couple weakly to this πN channel, they might not have been detected. Many quark models predict [6, 7] some resonances to have weak couplings to πN, but suggest they may be observed in γp reactions decaying to p$\pi\pi$ or pη, for instance. We may have failed to find the missing resonances simply because we have been looking in the wrong place.

Baryon resonances can be considered excited states of the 3-quark baryon ground state, roughly analogous to the excitation states of atomic electrons. Because of their very short lifetimes, on the order of 10^{-23} seconds, their widths are broad and difficult to determine. In contrast to the clear and distinct lines of optical spectra, the masses (lineshapes) of baryon resonances are described by wide and often overlapping Breit-Wigner functions. In order to identify any particular baryon resonance, it must be deconvolved from among other contributions.

Some reactions offer the distinct advantage of serving as an *isospin filter* for the spectrum of nucleon resonances and thus, simplifying the data interpretations and theoretical efforts to predict the excited states contributing to these reactions. The isospin-selective reaction $\gamma p \to \Delta\eta(I = 3/2) \to p\pi^0\eta$ facilitates the investigation of Δ^* states with masses above the effective reaction threshold. The analysis of this channel can help shed some light on the existence of Δ^* resonances with negative parity at about a mass of 1900 MeV/c^2, such as the $\Delta(1900)S_{31}$, $\Delta(1940)D_{33}$, and the $\Delta(1930)D_{35}$ (see Fig. 1.1). These states have at most a 3-star assignment by the Particle Data Group (PDG) and a confirmation of these poorly established states would contradict current constituent quark models, which predict them to be approximately 150-200 MeV/c^2 higher in mass.

Baryon resonances of higher mass (above 2 GeV/c^2), such as those we are investigating, are more likely to decay into particles of intermediate mass like the $\Delta(1232)$, rather than directly into the ground-state nucleon. Calculations for decays of these resonances into channels like Nπ, Nη, and Nω yield very small widths. High-mass states have total widths of at least 150 MeV/c^2, thus the remaining decays must be observed in reactions with higher thresholds. The investigation of p$\pi^0\eta$ is therefore advantageous in the search for yet unobserved states and preliminary results of the analysis are presented in this work.

This thesis has the following structure. Chapter 2 describes the experimental set-up used to accumulate the data for this work. A brief overview of the detector components is given. In chapter 3, the reconstruction and raw-data analysis of the data is presented. Preliminary differential cross-section results for the reaction γp $\rightarrow \Delta\eta \rightarrow$ p$\pi^0\eta$ are discussed in chapter 4 and further details of the general γp $\rightarrow$ p$\pi^0\eta$ analysis are given in chapter 5. The thesis ends with a brief summary and outlook.

Chapter 2

Experimental Set-Up

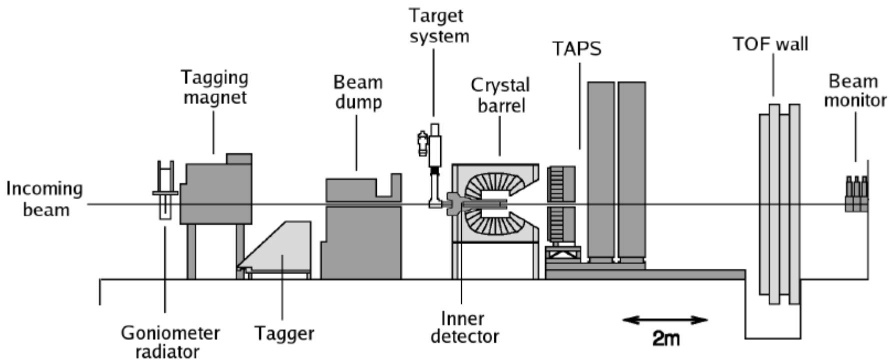

Figure 2.1: CB-ELSA/TAPS Experimental Set-up at ELSA. The initial electron beam enters from the left and hits a radiator target in front of the tagging magnet. Image courtesy of [10].

2.1 Introduction

The Crystal Barrel experiment is located at the **EL**ectron **S**tretcher **A**ccelerator (ELSA) facility in Germany and operated by the University of Bonn. It utilizes the ELSA electron beam and includes the photon tagging system, the liquid hydrogen target and two calorimeters which are optimized to detect multi-photon final states, permitting essentially full 4π solid-angle coverage of interactions (see Fig. 2.1). This experimental set-up is unique because other photoproduction experiments can mainly detect only charged final states while others have a small solid-angle coverage, or cannot reach the energy or beam intensity provided by ELSA.

The target in the center of the Crystal Barrel is a kapton cylinder 3 cm in diameter and 5.3 cm in length, with its long axis oriented along the beam line; the diameter is set by the beam spot size. Kapton is used because it is radiation resistant and relatively transparent to high-energy particles and photons. For the experiment presented here, it is filled with liquid hydrogen, and its temperature is controlled by recirculating the hydrogen through an external heat exchanger.

In the following sections, the different detector components are presented.

2.2 ELSA: ELectron Stretcher Accelerator

The acceleration of electrons proceeds via three stages (Fig. 2.2). Starting at one of two linear accelerators (LINAC), electrons are accelerated up to an energy of 20 MeV. The electrons are subsequently injected into the booster synchotron, where they receive further acceleration up to 1.6 GeV. Finally, the electron beam is transferred to the stretcher ring. The filling of the ring to the maximum allowed current and the acceleration takes approximately a second and the stored current is then extracted over a period of 8 seconds, called the spill, to the experiment. For the data presented here, ELSA supplied electrons to the Crystal Barrel experiment by slow extraction at a precisely controlled energy of 3.175 GeV.

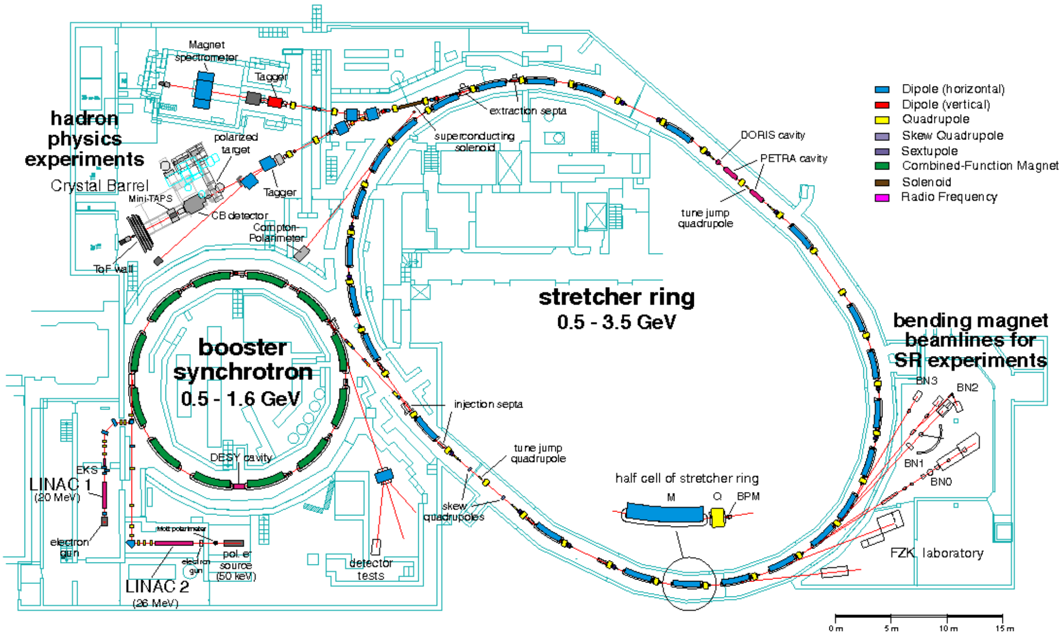

Figure 2.2: The accelerator complex at ELSA [11].

2.3 Tagging System

The tagging system permits the accurate determination of the energy of each incident photon, providing a tagged photon beam in the energy range from 750 to 2500 MeV, i.e. 25% - 95% of the incoming electron energy. Each electron from the ELSA accelerator passes through a copper radiator foil, where it is decelerated by the coulomb field of a copper nucleus and emits a photon by the bremsstrahlung process. The copper foil has a thickness of only 0.003 radiation lengths to preclude emission of multiple photons by one electron. The electron then passes a dipole magnet which bends it into a detector array. Electrons which do not undergo the bremsstrahlung process have a higher energy and are therefore deflected at a smaller angle, into a beam dump behind the detector.

The energy of the photon corresponds to the energy loss of the electron, which can be obtained from the measured deflection angle:

$$E_\gamma = E_0 - E_{e-} \tag{2.1}$$

While the electrons are of uniform energy, the photons produced by the bremsstrahlung process have a wide energy spectrum with the highest intensity at lower energies. To a first approximation, the intensity of the photon energy spectrum is inversely proportional to energy.

$$\Phi \sim \frac{1}{E_\gamma} \tag{2.2}$$

2.4 Inner Detector

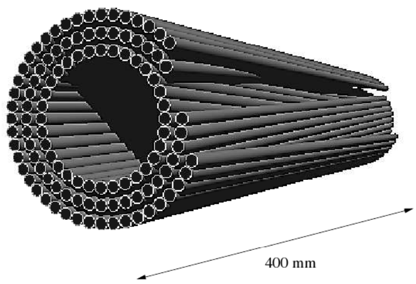

Figure 2.3: The scintillating fiber inner detector [12].

To detect charged particles leaving the target, a scintillating fiber detector was developed. The inner detector consists of 513 scintillation fibers in three layers arranged in a cylinder 40 cm long and about 11 cm in diameter. These fibers are bonded to lightguides leading to photomultipliers. The inner detector detects the passage of a charged particle above a threshold energy by the ionization trail it leaves in the scintillating material; as the electrons return to their ground state they emit photons in the visible spectrum, which are detected by photomultipliers. The path traversed by the particle through the fibers is a small fraction of the radiation length, so the particle is usually not absorbed and continues on to the outer detectors with its energy essentially unaffected. The fibers in each layer spiral about the support structure at $+22.5°$ and $-24.5°$; if a signal is detected in all three layers, their intersection identifies the point at which the particle passed through the detector. In past experiments the inner detector was utilized as a trigger; a signal (detected simultaneously in at least two fibers) indicated that a proton had been ejected from the target and was used to trigger the detection of a hadronic event.

2.5 Crystal Barrel Calorimeter

The Crystal Barrel [13] is one of the main components of the experiment, consisting in its 2002/2003 configuration of 1290 CsI crystals doped with thallium which enclose about

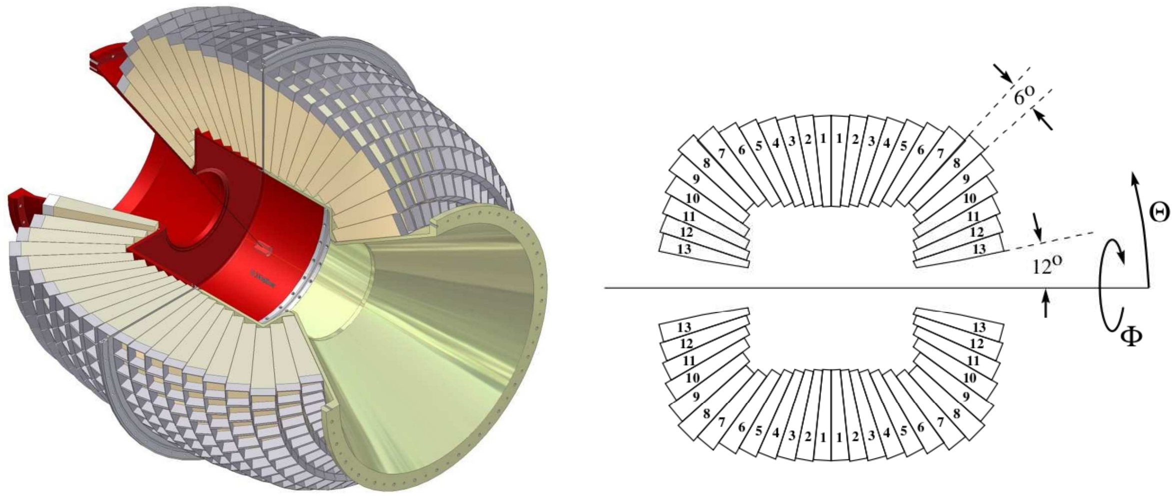

(a) Full view

(b) Cross section

Figure 2.4: The barrel-shaped Crystal-Barrel calorimeter. The CsI modules are organized in rings around the beam axis. For the experiment presented here, rings 11-13 (downstream) were removed.

80% of the total 4π solid angle. The modules have excellent photon detection efficiency. Figure 2.4 shows a cross section picture of the Crystal Barrel detector. A calorimeter is a detector which absorbs the full kinetic energy of a particle and provides a signal which is proportional to that deposited energy. This is accomplished by utilizing heavy elements, which limits the radiation length, and orienting the crystal so that the path length of the particle is much greater than the radiation length. Gamma rays entering the crystal initially undergo pair production. The created electron-positron pairs then loose energy by ionization. The Crystal Barrel detector crystals are 30 cm long, which corresponds to approximately 16 radiation lengths, permitting complete absorption of photons.

The majority of the absorbed energy is lost as heat, but a fraction is converted into visible-light photons which are detected by the photo-diode at the outer end of the crystal; thallium-doped cesium iodide has a very high scintillation efficiency of 52,000 photons/MeV which provides good sensitivity [14].

2.6 TAPS calorimeter

The Two-Armed Photon Spectrometer (TAPS) was developed for the MAMI [1] experiment and added to the Crystal Barrel experiment in 2002. The TAPS uses 528 hexagonal BaF_2 crystals in a planar array, with a thickness of about 12 radiation lengths (see Fig. 2.5). This detector was designed to identify specific charged and neutral particles through fast detector response and corresponding pulse shape analysis, and provides further discrimination by means of a 5 mm scintillation detector on the forward face of the crystals to identify charged particles. The TAPS is a fast detector and is utilized as a first-level trigger for the data

[1] MAMI = Mainzer Mikrotron, University of Mainz

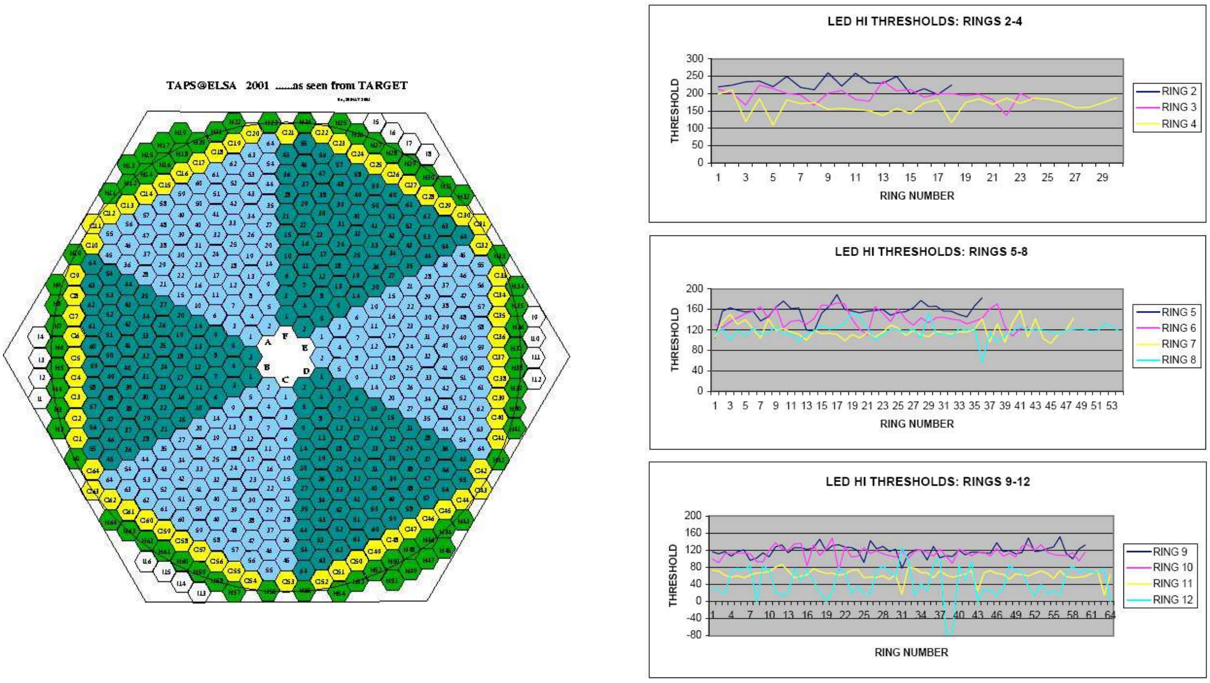

Figure 2.5: The TAPS detector [15] has 528 hexagonal crystals arranged in a planar array. Data on the particle energy thresholds of the individual crystals were compiled for this study and used to prepare new values relating detector threshold to distance from the axis.

presented in this study. Additionally, the TAPS increases angular coverage and provides high granularity in the forward direction, i.e. in the area around the downstream beam line, which is not covered by the Crystal-Barrel.

2.7 Triggering

The trigger identifies particular event topologies of interest for recording among the many signals detected. The trigger required either two hits above a low-energy threshold in the TAPS Leading Edge Discriminator (LED low) or one hit above a higher-energy threshold in TAPS (LED high) in combination with at least one cluster in the Crystal-Barrel calorimeter. The second-level trigger used a FAst Cluster Encoder (FACE) based on a cellular logic to define the number of contiguous clusters in the Crystal Barrel. The original values for the LED-thresholds fluctuated (see Fig. 2.5) and were difficult to simulate. For the analysis presented here, I established a new designation scheme, based on the distance of each BaF_2 crystal, or *ring* it belonged to. It was preferred that each ring have the same threshold in order to eliminate ϕ dependences, though too high a threshold would result in excessive loss of statistics. Ultimately, the crystals in a particular ring were assigned the highest threshold value for that ring.

Chapter 3

Data Analysis

Data for the analysis presented in this work were taken from October through November 2002 in two run periods with ELSA beam energies of 3.175 GeV. The data sets include approximately 720 million events.

3.1 Event Reconstruction

Reconstruction is the process of decoding the raw data in terms of electronic signals and extracting the four-momentum vectors (P_x, P_y, P_z, E) of measured particles. The four-momenta of the neutral mesons (π^0, η) cannot be measured directly but can be reconstructed from their decay products. A previously written C++ based routine was used to reconstruct the four-vectors of all the possible products.

The reaction under study is

$$\gamma \mathrm{p} \rightarrow \mathrm{p}\pi^0\eta \qquad (\pi^0,\, \eta \rightarrow \gamma\gamma) \tag{3.1}$$

and yields one π^0 and one η, each of which decays into two photons. Events with at most one proton and with four photons were selected. The charged clusters were identified in TAPS by using the plastic scintillators mounted in front of each BaF_2 crystal. The efficiency of these (photon)-veto detectors was determined and carefully modelled in the Monte-Carlo (MC) program. In the Crystal-Barrel reconstruction, a cluster is assigned to a charged particle if the trajectory from the target center to the barrel hit forms an angle of less than 20° with a trajectory from the target center to a hit in the scintillating fiber detector. Proton identification is only used to remove it from the list of photon candidates. The proton momentum is then reconstructed from event kinematics in “missing-proton” kinematic fitting. Proton clusters are on average much smaller than photon clusters and provide worse angular resolution. The proton momentum direction reconstructed from kinematic fitting had to be consistent again with a calorimeter hit when a charged cluster was identified.

Kinematic Fitting

Kinematic fitting uses the known physical constraints to slightly adjust the measured values, within their estimated error ranges, until they fulfil exactly the known constraints. The constraints that apply to this reaction include energy conservation:

$$E_\gamma + m_p = E_{p\prime} + \sum_{i=1}^{N_\gamma} E_{\gamma i}, \tag{3.2}$$

where E_γ is the incoming photon energy, $p\prime$ is the energy of the outgoing proton, and N_γ is the number of photons in the final state. The initial proton is assumed to begin at rest, so momentum conservation requires:

$$\overrightarrow{P_\gamma} = \overrightarrow{P_{p\prime}} + \sum_{i=1}^{N_{\gamma_i}} \overrightarrow{P_{\gamma_i}} \tag{3.3}$$

The invariant masses of the mesons are also used as constraints:

$$(E_{\gamma_1} + E_{\gamma_2})^2 = m_{\pi^0}^2 + (\overrightarrow{P_{\gamma_1}} + \overrightarrow{P_{\gamma_2}})^2 \tag{3.4}$$

$$(E_{\gamma_1} + E_{\gamma_2})^2 = m_\eta^2 + (\overrightarrow{P_{\gamma_1}} + \overrightarrow{P_{\gamma_2}})^2 \tag{3.5}$$

We must decide whether to accept each event as a reaction of the type $\gamma \mathrm{p} \rightarrow \mathrm{p}\pi^0\eta$. To accomplish this we measure the parameters and compare them to their expected values. For each parameter used in the hypothesis test there is a known correct value, a known standard deviation in our observations, and a measured value. For each parameter the normalized variance is calculated; the error (that is, the difference between the observation and the known correct value) is squared and divided by the variance of the measurement. The sum of these normalized variances, Q, has the χ^2 probability distribution. The shape of the χ^2 probability distribution depends only on the number of degrees of freedom, i.e. the number of different parameters measured, and has the PDF of the sum of the squares of k independent, normally distributed variables with mean 0 and standard deviation 1.

$$Q = \sum_{i=1}^{k} x_i, \tag{3.6}$$

For a set of observations x_i with known values u_i, we can calculate χ^2, which is then minimized in the kinematic fit procedure:

$$Q = \sum \frac{(x_i - u_i)^2}{{\sigma_i}^2} \sim \chi^2 \tag{3.7}$$

Verification of the Kinematic Fit

To make judgements and decisions about the *goodness* of the fit, the relevant quantity is the integral:

$$CL(\chi^2) \;=\; \int_{\chi^2}^{\infty} P(\chi^2; n)\, d\chi^2 \;, \tag{3.8}$$

which is called the χ^2 *likelihood* or confidence level. If χ^2 is large, so that $P(\chi^2)$ is small, it could be that the errors are underestimated or that the initial hypothesis was wrong. The kinematical fit is an ideal method to judge possible final-state hypotheses for an event. Figure 3.1 shows a typical confidence-level distribution.

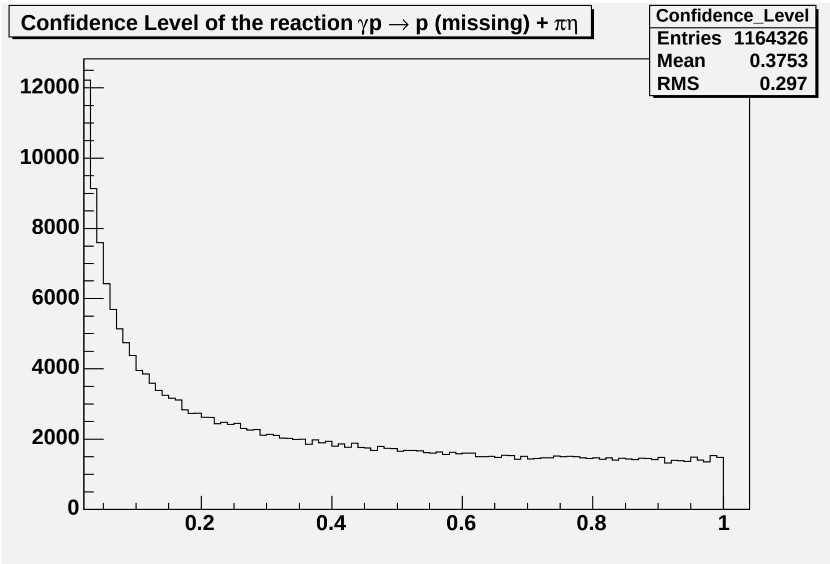

Figure 3.1: Confidence level distribution for the reaction $\gamma\text{p} \rightarrow \text{p}\pi^0\eta$. Background events generally have low confidence levels, indicated by the sharp rise below $CL = 0.2$. When making selection cuts, a compromise must be reached between a very tight cut (which eliminates more background at the expense of statistics) and a very loose cut (which is likely to incorrectly accept background events).

If errors have been estimated correctly, than the χ^2 distribution of the fitted events will approximate the standard χ^2 distribution. In this case, the confidence level measurements will fit a uniform (flat) distribution with a range from 0 to 1, which suggests 1) that the calculation of χ^2 is accurate, i.e. that the estimates of error in each of the measurements are accurate, and 2) that most of the accepted events have been correctly identified. Background events will have a low confidence level and can be rejected by a cut. We inspected the distribution of confidence limits and found that it did indeed approximate the uniform distribution.

An additional test to verify the accuracy of the kinematic fit is to inspect the distribution of the "pulls", i.e. the changes made to the data during the fitting process. A random error is just as likely to be positive as negative, so the average value of the errors should be zero, and their standard deviation should be the standard deviation assumed in estimating the accuracy of the measurement. If the distribution of errors is normalized to this value, the result should be a Gaussian with $\sigma = 1$. This is called the pull distribution:

$$P_i = \frac{\eta_i - \eta_f}{\sqrt{\sigma^2_{\eta_i} - \sigma^2_{\eta_f}}} \tag{3.9}$$

A larger standard deviation indicates that the errors are greater than were estimated, while a standard deviation smaller than one indicates the errors are less than predicted. If the mean is significantly different from zero it suggests there were systematic errors in the measurement. The distribution of the pulls (Fig. 3.1) was checked and found to be appropriate.

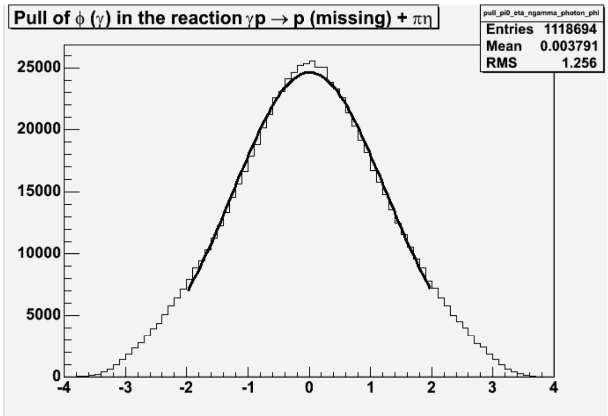

Figure 3.2: Pull distribution for ϕ.

3.2 Monte Carlo Simulations

The performance of the detector was simulated in GEANT3-based Monte Carlo studies. The program package used for CB-ELSA/TAPS is built upon a program developed for the CB-ELSA experiment. The Monte Carlo program reproduces accurately the response of the TAPS and Crystal Barrel crystals when hit by a photon. For charged particles, the detector response is known to a lower precision but still reasonably well understood.

The acceptance for the reaction (3.1) was determined by simulating events, which were evenly distributed over the available phase space. The Monte Carlo events were analyzed using the same reconstruction criteria, which were also applied to the (real) measured data. The same hypotheses were tested in the kinematic fits and events selected with the same confidence level cuts. The acceptance is defined as the ratio of the number of generated and reconstructed Monte Carlo events

$$A_{\gamma\mathrm{p}\to X} = \frac{N_{\mathrm{rec,MC}}}{N_{\mathrm{gen,MC}}} \qquad (X = \Delta\eta,\ \text{for instance}). \tag{3.10}$$

The trigger required either two hits above a low-energy threshold in TAPS (LED low – Leading-Edge Discriminator threshold) or one hit above a higher-energy threshold in TAPS (LED high) in combination with at least one cluster in the Crystal Barrel calorimeter. The second-level trigger used a FAst Cluster Encoder (FACE) based on a cellular logic to define the number of contiguous clusters. The decision time depended on the complexity of the hit distribution in the Crystal Barrel and was typically 4 μs. In case of an event rejection, a fast reset was generated, which cleared the readout electronics in 5 μs. Otherwise the readout of the full event was initiated with typical readout times of 5-10 ms. To properly simulate the detector response, FACE and TAPS-LED thresholds had to be determined from the data for all crystals. Given the different response characteristics of protons and photons in $\mathrm{BaF_2}$ crystals, protons experience slightly different LED-thresholds than photons. For this reason, we have corrected the measured proton energy according to $0.8 \cdot E_\mathrm{p} + 30$ MeV, which is derived from available proton times in TAPS and from Monte Carlo studies. At the reaction threshold, when the proton is required in the (TAPS) trigger, corrections are small. Our understanding of the threshold function is fair to good and reasonably well reproduced in the trigger simulation.

Chapter 4

Analysis of $\gamma p \rightarrow \Delta^+(1232)\eta \rightarrow p\pi^0\eta$

The analysis of the photo-produced $p\pi^0\eta$ final state requires five independent kinematic variables and is thus difficult because the extraction of cross-sections for a 3-body final state requires a CPU- and (real) time-consuming 5-dimensional acceptance correction. Though certainly possible this goes beyond the scope of this work.

For this reason, the reaction $\gamma p \rightarrow p\pi^0\eta$ reaction is reduced in a first step to a 2-body final state:

$$\gamma p \rightarrow \Delta\eta \rightarrow (p\pi^0)\eta. \tag{4.1}$$

The full kinematic description of a 2-body final state requires only two independent variables, which are traditionally chosen to be the incoming photon energy E_γ and $\cos\theta$ of the meson in the center-of-mass system. The goal of this undergraduate thesis work is to determine preliminary $\Delta\eta$ differential cross sections. The angular shape of such cross sections will guide further efforts to understand the production mechanisms leading to this final state. The method used here is to fit the $p\pi^0$ mass projections from the initial $p\pi^0\eta$ final state to determine the Δ yields for all $(E_\gamma, \cos\theta)$ bins.

The reconstruction of the final-state 4-vectors has been outlined in section 3.1. Section 4.1 describes the experimental mass distributions and the fit method. In section 4.2, first results of the fits are discussed and the underlying limits of our method to extract the reaction yields. The Δ resonance is a broad resonance and uncertainties in the background shape of the distributions certainly render difficult an accurate extraction of reaction yields. Finally, section 4.3 presents the differential cross sections and explains how they were experimentally determined.

4.1 Fitting the $p\pi^0$ Mass Spectra

The $p\pi^0\eta$ events are reconstructed from four-photon events, which have been kinematically fitted to the hypothesis:

$$\gamma p_{\text{missing}} \rightarrow p\eta\gamma\gamma. \tag{4.2}$$

A confidence-level cut at 10 % was applied for the simultaneously fitted $\pi^0\eta$ hypothesis as well as an anti-cut for the $\pi^0\pi^0$ hypothesis at the 1 % level to reduce background. Figure 4.1 (left side) shows the invariant $\gamma\gamma$ mass of the remaining photon pair. A nice π^0 peak is clearly visible above a very small background of less than 5 %. An alternative method of reconstructing the $p\pi^0\eta$ final state is provided by fitting the events to $\gamma p_{\text{missing}} \rightarrow p\pi^0\gamma\gamma$.

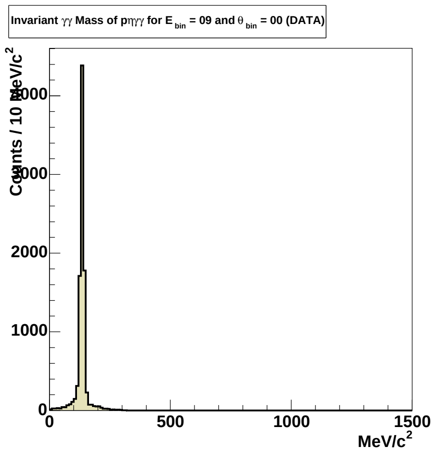

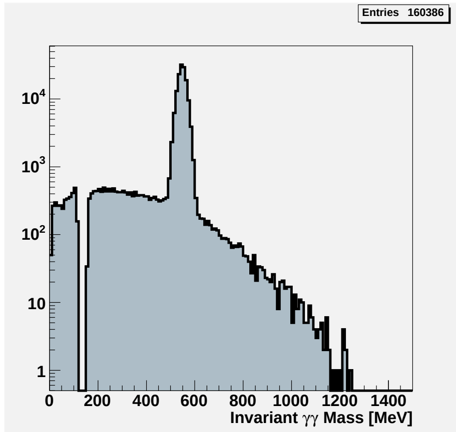

Figure 4.1: Invariant $\gamma\gamma$ mass distributions for four-photon events fitted to the $\gamma p_{\text{missing}} \to p\eta\gamma\gamma$ hypothesis (left side) and $\gamma p_{\text{missing}} \to p\pi^0\gamma\gamma$ (right side). Background due to the competing reaction $\gamma p \to \pi^0\pi^0$ was reduced by applying CL cuts (see text for details). Signals due to $\pi^0\eta$ are clearly observed above very little background.

In this case, an η needs to be reconstructed from the invariant $\gamma\gamma$ mass. This distribution is shown in Fig. 4.1 (right side) from an earlier stage of the analysis, where a logarithmic scale for the vertical axis was chosen. The π^0 *hole* is due to a $\pi^0\pi^0$ confidence-level anti-cut in the analysis. Again, note the very small background underneath the η peak.

The events identified as $p\pi^0\eta$ were then categorized into bins according to the energy E_γ of the incident photon and the θ angle of the η meson in the center-of-mass system. We used 32 energy bins from $E_\gamma = 900$ to 2500 MeV with intervals of 50 MeV, although the lowest 7 bins were not used because they were below the $\Delta^+(1232)\eta$ reaction threshold of $E_\gamma \approx 1220$ MeV. We used 20 cos θ^η_{cm} angle bins over the range from 0 to 180°. A total of 500 bins had useful data (i.e. enough statistics). For each bin, the invariant $p\pi^0$ mass distribution of the $p\pi^0\eta$ system was histogrammed.

We know from a previous $p\pi^0\eta$ analysis of a (much) smaller CB-ELSA data set [16] that the major decay modes (Fig. 4.2) for N* and Δ^* isobars contributing to reaction $\gamma p \to p\pi^0\eta$ are considered to be

1. $\gamma p \to \Delta(1232)\eta \to p\pi^0\eta$
2. $\gamma p \to N(1535)S_{11}\pi^0 \to p\pi^0\eta$, and
3. $\gamma p \to pa_0(980) \to p\pi^0\eta$.

Thus, in the $p\pi^0$ invariant mass distribution we expect to see a dominant peak for the $\Delta(1232)$, plus the Dalitz-plot "projections" of the $N(1535)S_{11}$ and a_0 from the $p\eta$ and $\pi^0\eta$ invariant mass distributions, respectively. This can be seen in the $p\pi^0\eta$ Dalitz plot (Fig. 4.3, right side).

A Monte Carlo (MC) simulation of all the reactions above was used to generate a very large number of events, which were analyzed in the same energy/angle intervals as the actual data. The MC provided the expected mass spectra for these three channels in each of the 500 energy/angle bins; I then created probability density functions (PDFs) from each MC spectra.

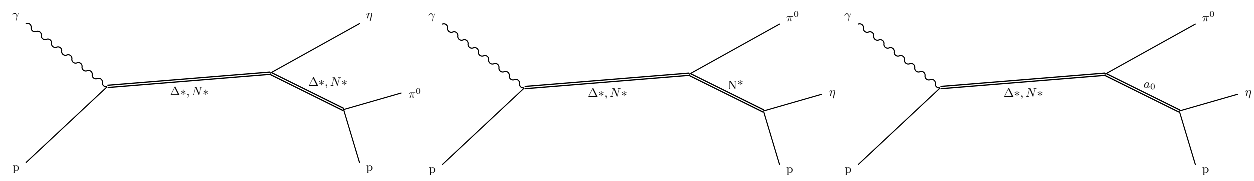

Figure 4.2: Resonant contributions to $\gamma p \rightarrow p\pi^0\eta$.

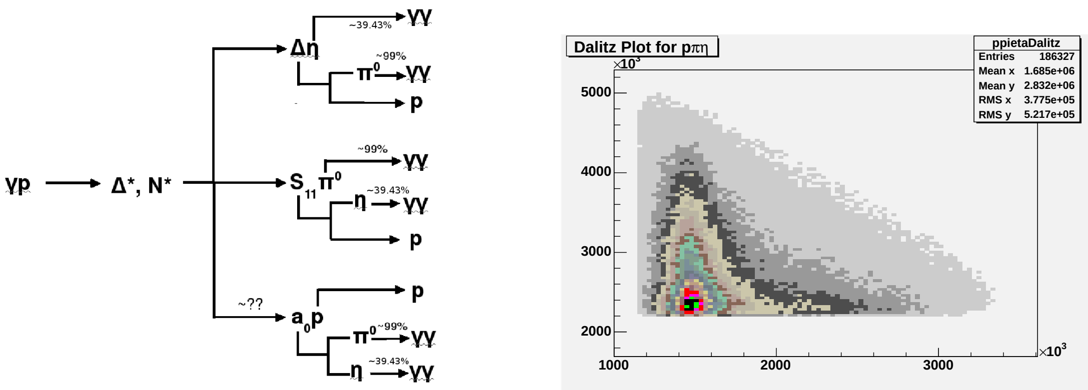

Figure 4.3: The left side shows the dominant N* and Δ^* decay modes leading to a $\mathrm{p}\pi^0\eta$ final state. Some branching fractions are also given. The right side shows the $\mathrm{p}\pi^0\eta$ Dalitz plot integrated over the available energy range. Dominant bands for the $\Delta(1232)$ (vertical) and the $\mathrm{S}_{11}(1535)$ (horizontal) can be clearly observed.

The major focus of my work was the fitting of the measured mass spectra to a linear function of these PDFs;

$$M_E = N_\Delta \cdot PDF_\Delta + N_{S_{11}} \cdot PDF_{S_{11}} + N_{a_0} \cdot PDF_{a_0}, \tag{4.3}$$

where M_E is normalized to $N_\Delta + N_{S_{11}} + N_{a_0} = N_{tot}$. I used the ROOFIT data modeling toolkit [17] to identify the optimal contributions. ROOFIT is an extension of the ROOT data analysis framework [18, 19] developed by Wouter Verkerke, which provides built-in classes that perform so-called *likelihood* fits by minimizing the negative log likelihood, or NLL (see next section for more details). ROOFIT provides the option of using an extended likelihood fit, normalizing the sum of the PDFs to the total number of events, thus generating fit curves for each PDF that are scaled to match the data histogram. A ROOT C interpreter script was written to perform this for each of the histograms.

Testing the Goodness of Fit

Much of scientific research consists of constructing a model, or hypothesis, and confronting it with experimental data to see how well it predicts or explains the observed findings. Any procedure of this sort requires a comparison of the likelihood that the observed data could have occurred by chance with the probability that it could have occurred given that the hypothesis is correct. This term *likelihood* is generally used, rather than probability, because the actual truth or falsehood of the hypothesis is not a random variable; in reality a hypothesis is either always true or always false, although we may have no way of knowing which is the case.

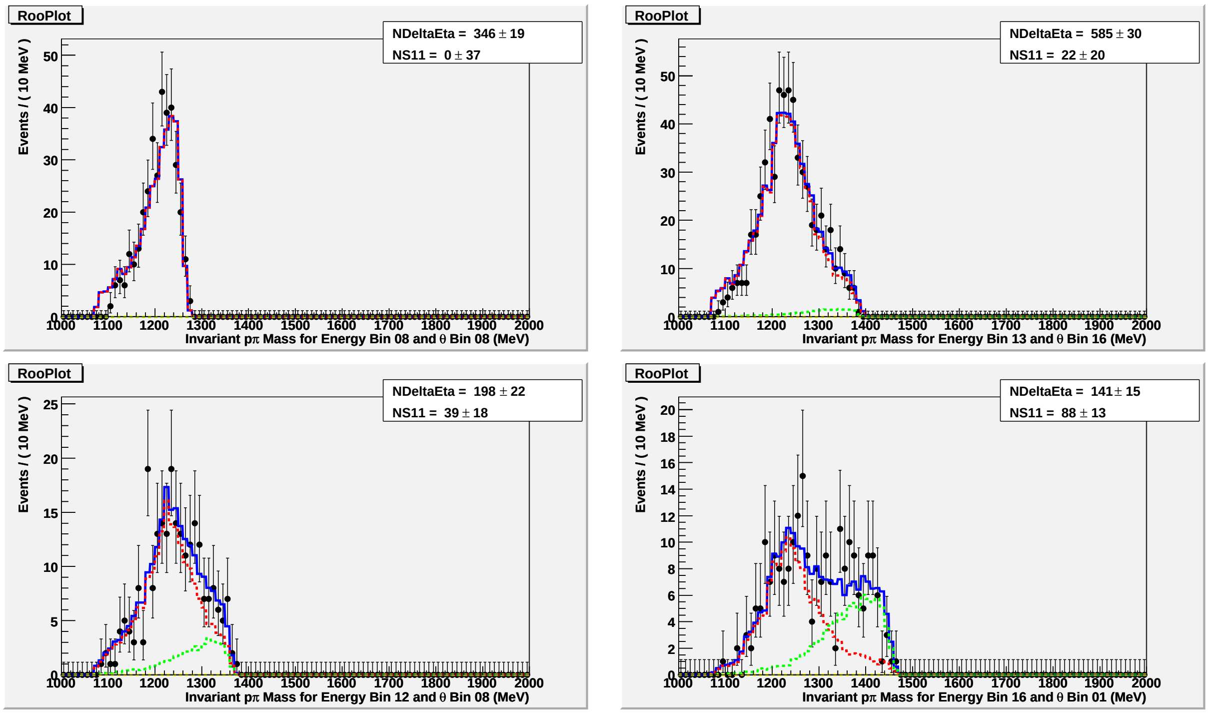

Figure 4.4: Examples of $p\pi^0$ invariant mass spectra, fit with a total PDF (blue), which is sum of the S_{11} (green) and Δ (red) contributions from the Monte Carlo model. In some cases at low energies, the fit optimizes without any S_{11} contribution.

When ROOFIT is used to fit one or more PDFs to a histogram, it uses a maximum likelihood procedure to optimize the magnitudes of the contributing PDFs; we need a way to evaluate how well the PDF fits the data. The method used by ROOFIT to select the most likely values for fitting parameters is called the negative log likelihood, or NLL, and this is recommended here as the best method to test the hypothesis or assess goodness of fit [17]. While a number of likelihood measures are available for testing a single application of a hypothesis, in ROOT it is often necessary to test a hypothesis simultaneously against a large number of data sets. Procedures that require the multiplication of many small probabilities can result in underflow errors [20]. If the natural log of each likelihood estimate is taken first, the logs can then be added for a composite likelihood estimate. If a likelihood is between 0 and 1, its log will be between minus infinity and zero. The term Negative Log Likelihood is something of a misnomer; the log likelihood would nominally be negative, so to simplify reporting its sign is reversed, hence it is negated. Consequently the reported value of the NLL is positive, with a smaller positive value indicating a greater likelihood. We used the sum of the NLL values for all energy/angle bins as a measure of the overall goodness of fit for each fitting method.

4.2 Adjustments to the Fitting Process

A large variety of fits for different energy bins is shown in Figures 4.7 - 4.10.

ROOFIT fits each histogram independently, based solely on the shapes of the contributing PDFs. As a result substantial errors were encountered in the fitting process, particularly in energy bins where the number of events was small, and in cases where the PDFs of different channels were similar in shape. In particular, the Na_0(980) contribution, which is known to be quite small, was sporadically indicated as very high. An attempt was made to improve the fit by limiting it to only 30 % of the total, however this proved ineffective, and ultimately it was necessary to remove the Na_0(980) contribution from the fit. The lower NLL value after this procedure confirmed that the fit was more accurate with only the Δ(1232) and N(1535)S_{11} contributions included.

Similarly, in six cases in bins 7 to 12, where the major contribution was clearly from the Δ(1232) channel, the fitting process ascribed almost the entire contribution to the N(1535)S_{11}. Geometrically, this error is understandable, as the two PDFs are very similar in shape at this point. However, it is known that at these energies the contribution of the N(1535)S_{11} channel is small, and it was clear from the histograms of the adjacent energy bins that the events were actually due almost entirely to the Δ(1232) channel.

The limitations in our fit procedure and the reason for some of the above failures are due to our choice of a naive *sum of Breit-Wigners* model to fit the $\mathrm{p}\pi^0$ mass projections. This model certainly does not account for additional resonance contributions, though small, or interference effects. The Breit-Wigners used in this analysis are provided by Monte Carlo distributions and thus, corrected for phasespace and relativistic effects.

Some residual errors remain, further indicating the limits of our yield extraction method:

- Background events incorrectly accepted, and
- t- and u- channel production, in which the proton and photon exchange a meson rather than actually forming a *s*-channel resonance. Because we have no way of precisely modeling these effects in the Monte Carlo or through an analytic function, at this time they cannot be further reduced.

4.3 Generating the Differential and Total Cross Sections

The Δ yields $N_{i,j}$ for each energy/angle bin (i,j) were calculated by integrating the fitted curve for the histogram. The differential cross section for the reaction $\gamma\mathrm{p} \rightarrow \Delta\eta$ is then determined experimentally according to:

$$\frac{\mathrm{d}\sigma}{\mathrm{d}\Omega} = \frac{N_{\gamma\mathrm{p}\rightarrow\Delta\eta}}{A_{\gamma\mathrm{p}\rightarrow\Delta\eta}} \frac{1}{N_\gamma \rho_\mathrm{t}} \frac{1}{\Delta\Omega} \frac{1}{BR_{\pi^0\rightarrow\gamma\gamma}} \frac{1}{BR_{\eta\rightarrow\gamma\gamma}} \frac{1}{BR_{\Delta\rightarrow p\pi^0}}\,, \tag{4.4}$$

where

$$\begin{aligned}
\rho_\mathrm{t} =& \quad \text{target area density} \\
N_{\mathrm{X}\rightarrow\Delta\eta} =& \quad \text{number of reconstructed } \Delta\eta \text{ events} \\
& \quad \text{in an } (E_\gamma, \cos\theta_\mathrm{cm}) \text{ bin (extracted from fit)} \\
N_\gamma =& \quad \text{number of photons in an } E_\gamma \text{ bin} \\
A_{\mathrm{X}\rightarrow\Delta\eta} =& \quad \text{acceptance in an } (E_\gamma,\, \cos\theta_\mathrm{cm}) \text{ bin} \\
\Delta\Omega =& \quad \text{solid–angle interval} = 2\pi\cos(\theta_{cm}) \\
BR =& \quad \text{decay branching ratio.}
\end{aligned}$$

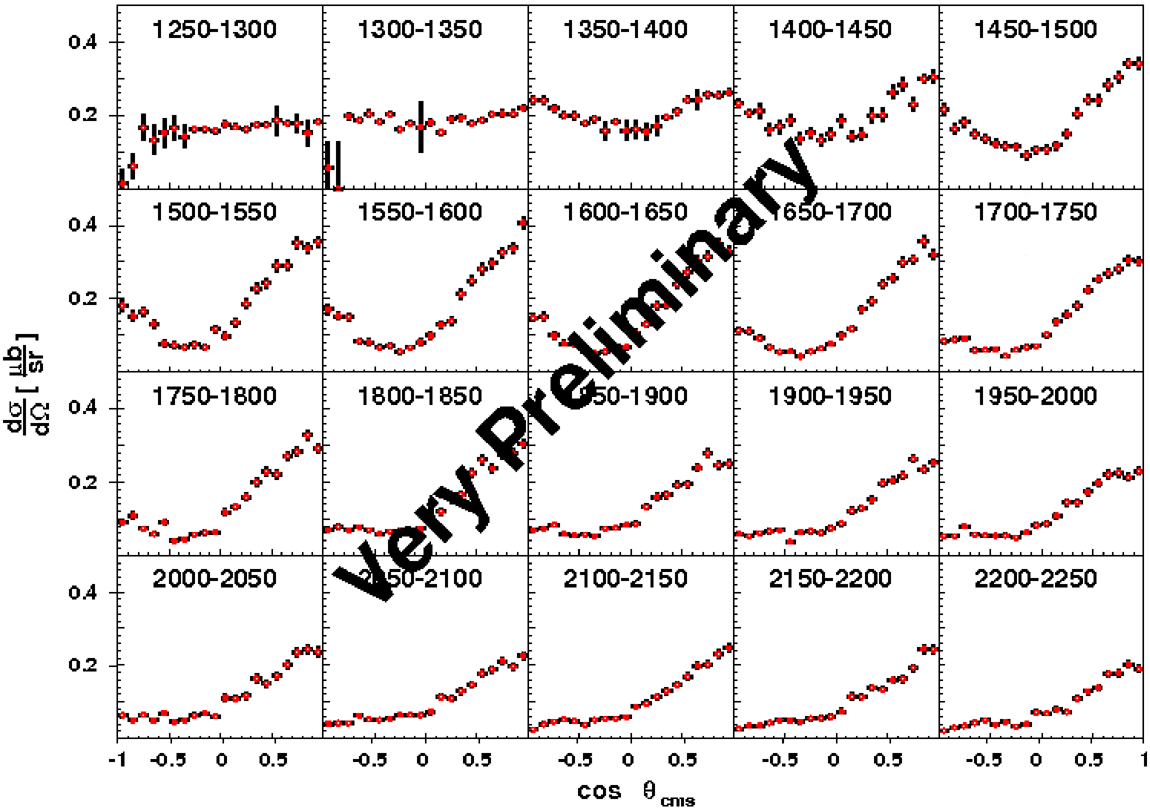

Figure 4.5: Differential Cross Sections for the reaction $\gamma\mathrm{p} \to \Delta\eta$ from close to the reaction threshold at 1500 to 2500 MeV. Error bars are only statistical. The angular distributions are flat close to threshold and develop a forward peak at higher energies indicating t-channel exchange mechanisms. Resonance contributions are observed over the full energy range.

The target area density is the number of protons per cross sectional area of the target, orthogonal to the photon beam. This value is given by:

$$\rho_{\mathrm{t}} = 2\,\frac{\rho(\mathrm{H}_2)N_{\mathrm{A}}L}{M_{\mathrm{mol}}(\mathrm{H}_2)} = 2.231 \cdot 10^{-7}\mu\mathrm{b}^{-1}, \tag{4.5}$$

where $\rho(\mathrm{H}_2) = 0.0708\,\mathrm{g/cm}^3$ is the density and $M_{\mathrm{mol}} = 2.01588\,\mathrm{g/mol}$ the molar mass of liquid H_2. $N_{\mathrm{A}} = 6.022 \cdot 10^{23}\,\mathrm{mol}^{-1}$ is the Avogadro number and $L = 5.275\,\mathrm{cm}$ the length of the target cell. The factor of two accounts for the molecular composition of hydrogen, H_2.

The differential cross sections for the reaction $\gamma\mathrm{p} \to \Delta\eta$ are shown in Fig. 4.5. Only statistical errors are included at this point. The cross sections are given in 50-MeV wide energy bins and in 20 $\cos\theta$ bins per corresponding energy bin. The angular distributions are absolutely normalized from the experimental data.

The data cover the full angular range. A flat angular distribution is observed at low energies suggesting s-channel resonance production near threshold. The dataset shows a continuing increase in slope at forward angles, which becomes more dominant at higher energies. This forward peak is most likely due to t-channel exchange mechanisms. Moreover, our data indicate a decrease in the forward most bin as expected from t-channel contributions.

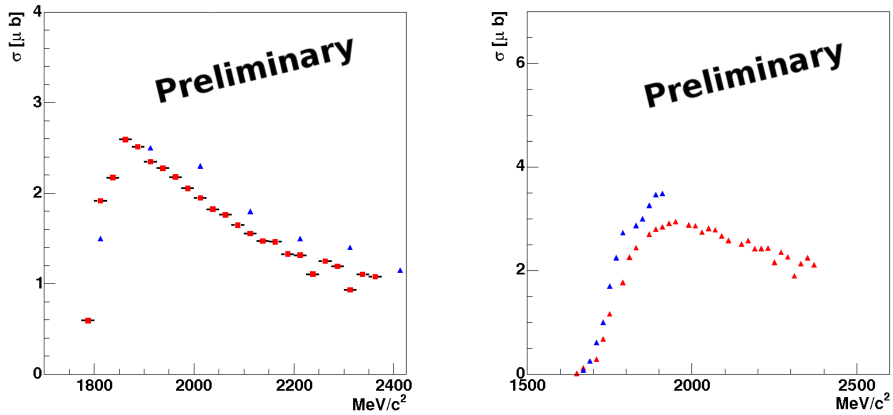

Figure 4.6: The left side shows the total cross section for the reaction $\gamma p \rightarrow \Delta\eta$ (■). The triangles (▲) represent a previous CB-ELSA analysis, which was based on a data set with an order of magnitude less statistics. The right side shows a very preliminary total cross section of $\gamma p \rightarrow \pi^0\eta$ (red ▲) (see chapter 5 for more details). The blue triangles (▲) show results from the GRAAL experiment.

Above 1400 MeV in photon energy, growth at backward angles is observed suggesting u-channel contributions. This growth seems to flatten out again above 1800 MeV and needs to be treated very carefully; this feature is usually not observed close to threshold. It could be underestimated background underneath the Δ peak in the mass distributions due to increasing N(1535)S_{11} contributions. At these incoming photon energies, the S_{11} occurs as a fairly symmetric background around the Δ mass (figure 4.7), whereas a cleaner separation is possible at higher energies (figure 4.10).

The large statistical fluctuations in the backward region close to threshold (1250 - 1300 MeV) are due to very low statistics in the $p\pi^0$ mass distributions.

The total cross section is calculated by integrating over the differential cross sections:

$$\sigma = \int d\Omega \, \frac{d\sigma}{d\Omega} \tag{4.6}$$

and shown in Fig. 4.6 (left side). The overall agreement with the results of the previous CB-ELSA analysis is fair. Though the overall shape resembles the previous findings, the absolute magnitude is on the average approximately 20 % smaller. The right side of figure 4.6 shows the very preliminary total cross for the reaction $\gamma p \rightarrow p\pi^0\eta$ (red triangles) and for comparison, results from the GRAAL experiment in France (blue triangles). Again, the agreement of shapes is fair to good, the total magnitude is smaller. It's worth noting that the peak of the $\Delta\eta$ cross section at about 2.5 μb almost matches the maximum in the total $\pi^0\eta$ cross section. This indicates that Δ^* production dominates the $\pi^0\eta$ final state below incoming photon energies of $E_\gamma < 2$ GeV.

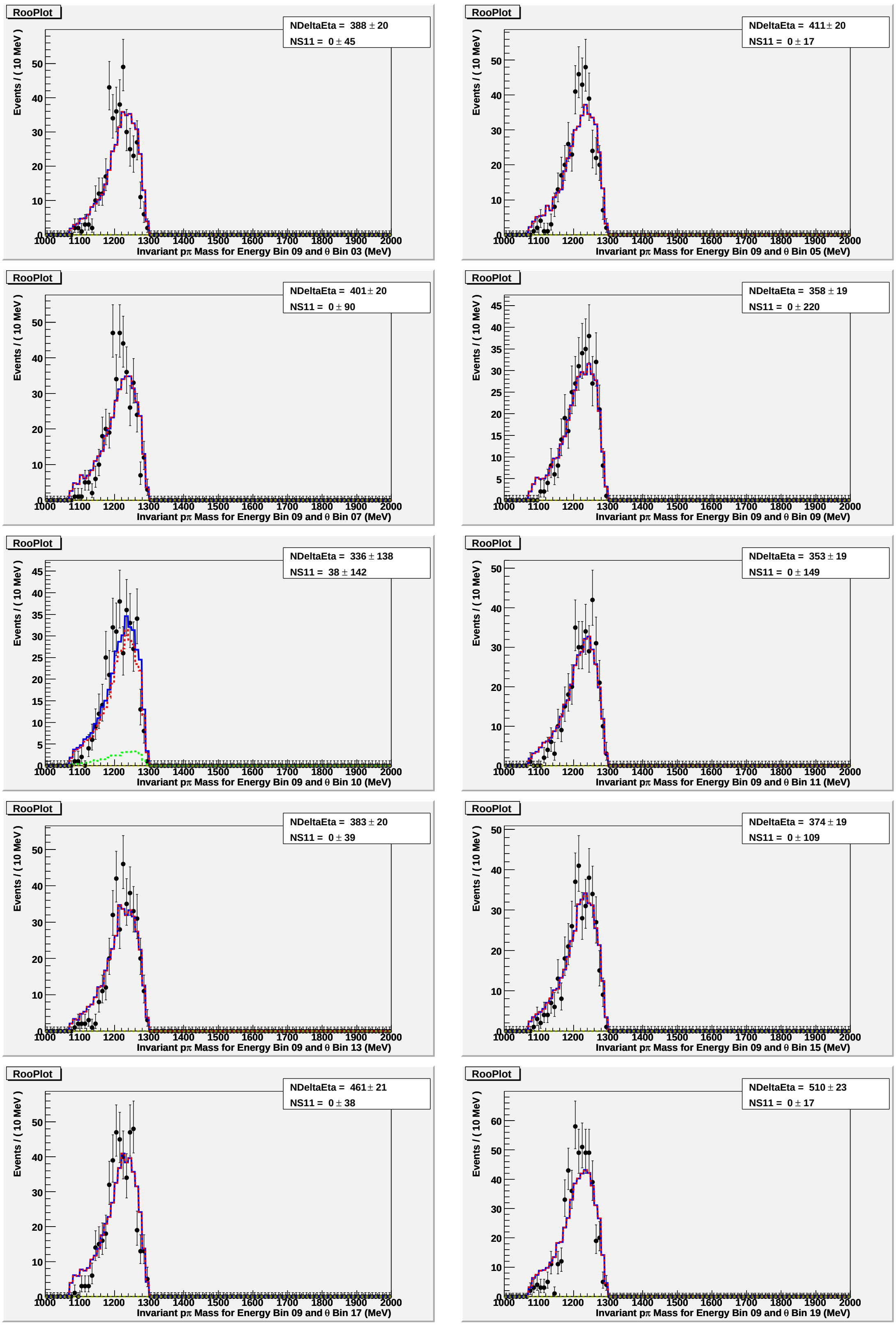

Figure 4.7: Example $p\pi^0$ invariant mass spectra from energy bin 9 (1350-1400 MeV). Spectra are fit with a total PDF (blue), which is sum of the S_{11} (green) and Δ (red) contributions from the Monte Carlo model.

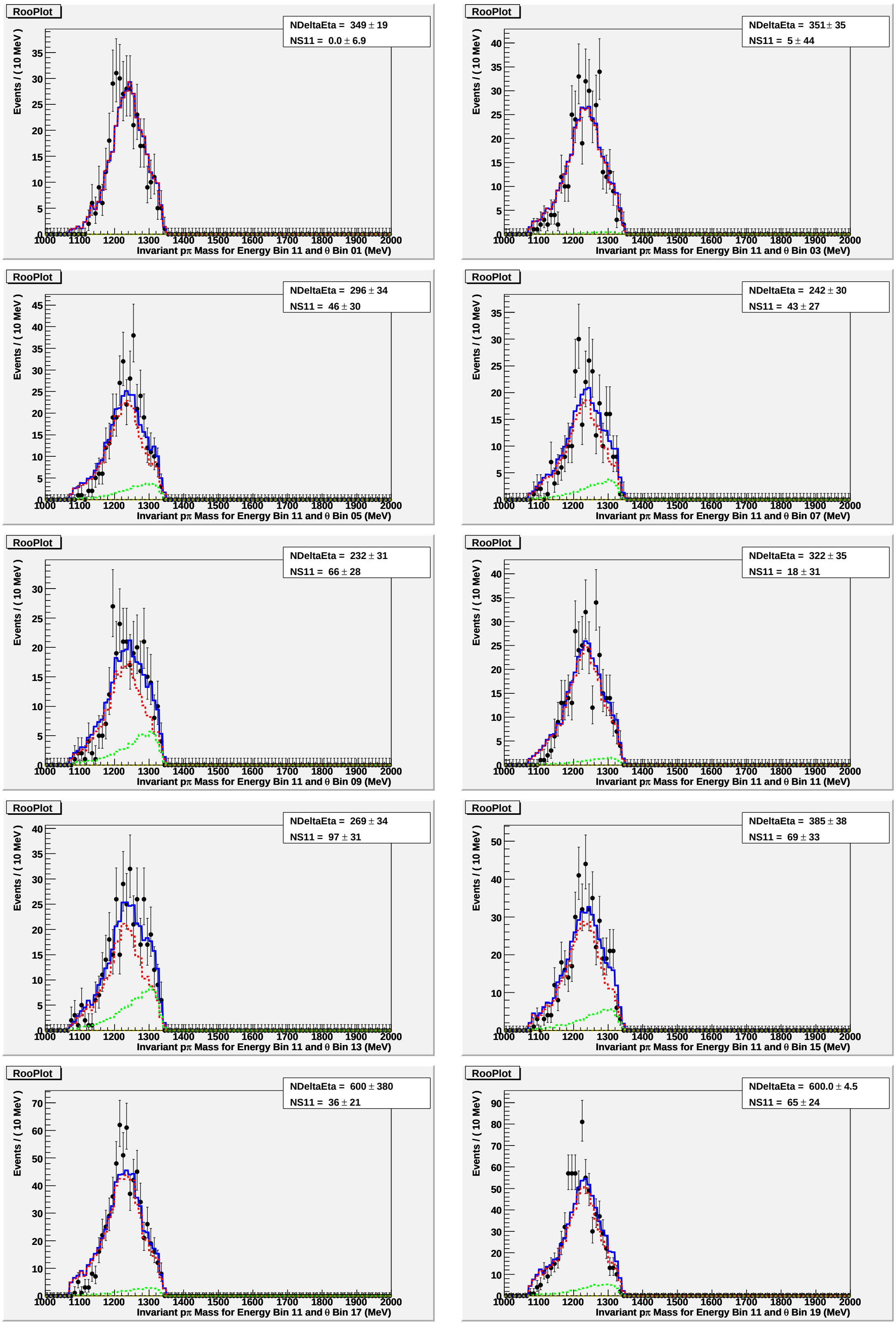

Figure 4.8: Example $\mathrm{p}\pi^0$ invariant mass spectra from energy bin 11 (1450-1500 MeV). In some cases, the fit optimizes without any S_{11} contribution.

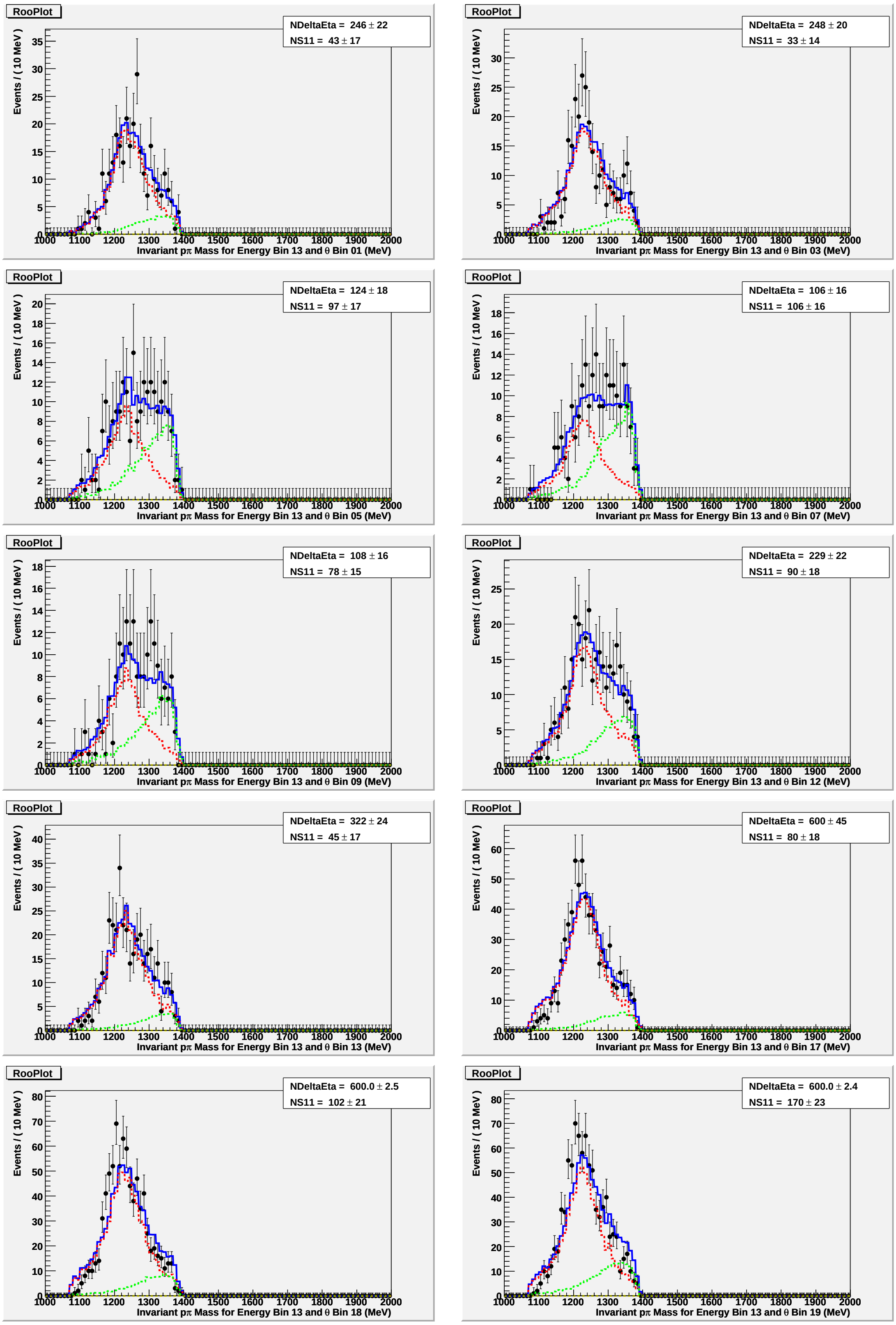

Figure 4.9: Example $p\pi^0$ invariant mass spectra from energy bin 13 (1550-1600 MeV). The development of a second peak next to the Δ peak becomes visible.

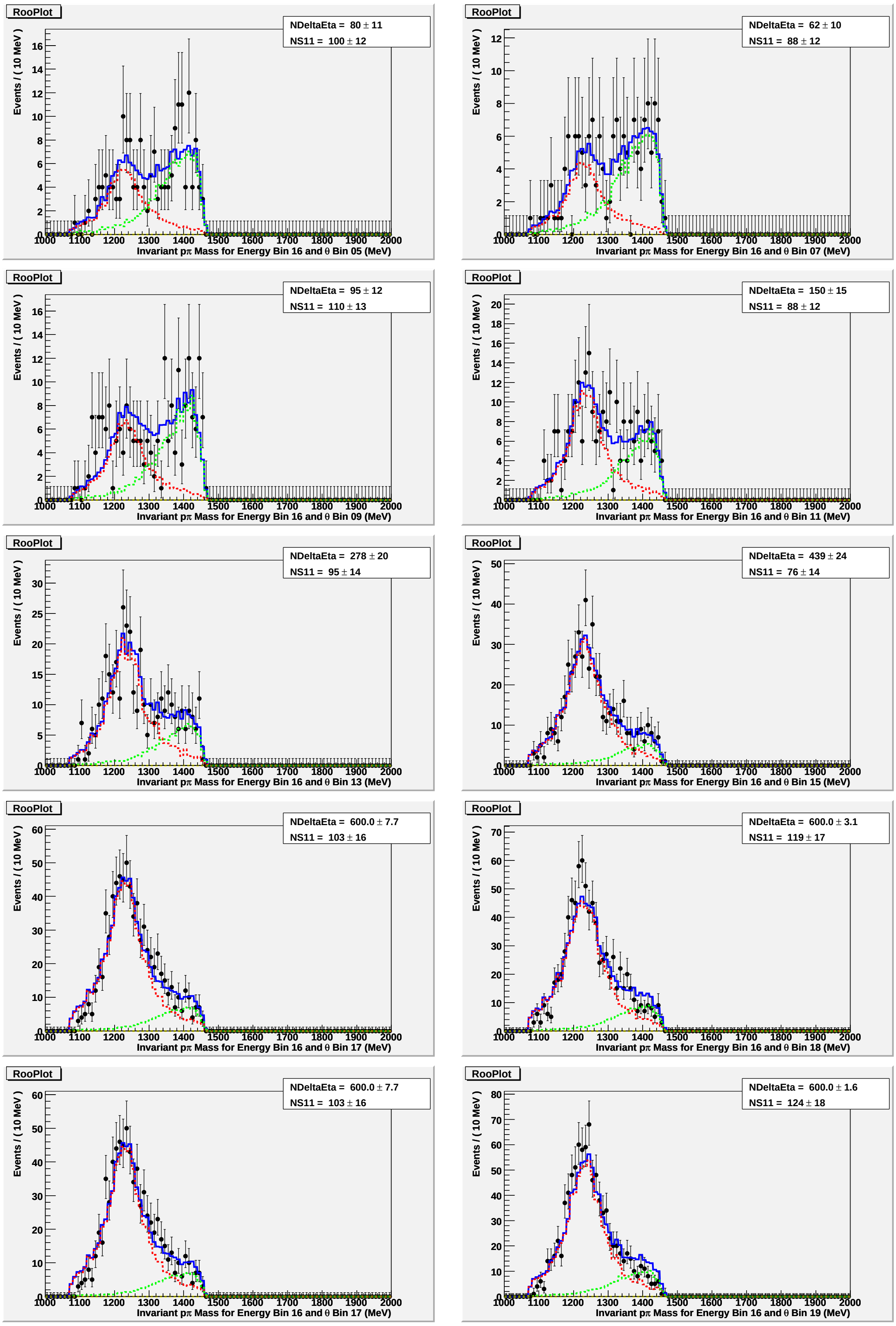

Figure 4.10: Example $p\pi^0$ invariant mass spectra from energy bin 16 (1700-1750 MeV). The distributions indicate the dominant production of $\Delta\eta$ in the forward direction (center-of-mass system).

Chapter 5

Analysis of $\gamma p \to p\pi^0\eta$

In chapter 3, the reconstruction and preparation of a $\pi^0\eta$ data set was briefly described. Approximately 186,000 $\gamma p \to p\pi^0\eta$ events were identified, an order of magnitude more events than were accumulated in an earlier experiment [16]. Moreover, these data cover the full angular range and thus in principle allow a model-independent extraction of cross sections. Unfortunately, this procedure requires a huge amount of Monte Carlo statistics and was not possible for this work. The next section discusses the basic method and presents a first preliminary result.

5.1 The System of Coordinates

As described in [21], the reaction is described relative to two planes, both with their origin at the center of mass (Fig. 5.2). The scattering plane contains the paths of the incident and scattered proton, while the decay plane contains the paths of the scattered proton, the pion, and the η meson. The two planes intersect along the path of the scattered proton. The angle between them, ϕ^*, at first glance appears to be a parameter of the reaction, but in fact the other parameters of the reaction are independent of it.

Figure 5.1 shows two-dimensional plots of Φ^* versus Θ^* (as defined in Fig. 5.2), inte-

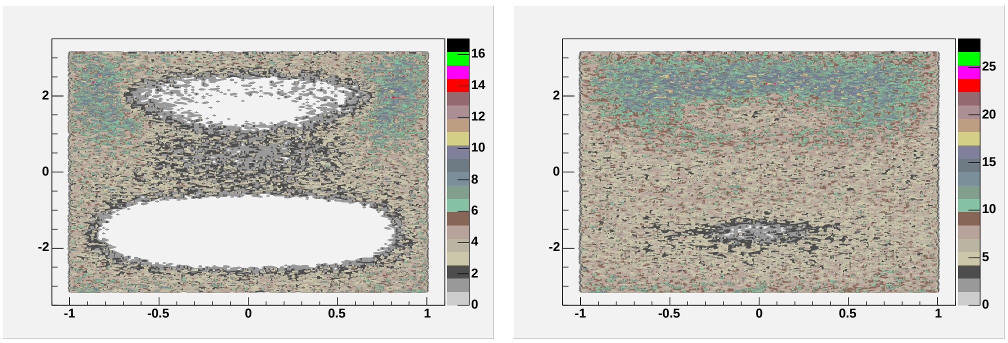

(a) Previous CB-ELSA analysis. (b) Current work (CB-ELSA/TAPS).

Figure 5.1: Two-dimensional plots of Φ^* versus Θ^*, integrated over all incoming photon energies.

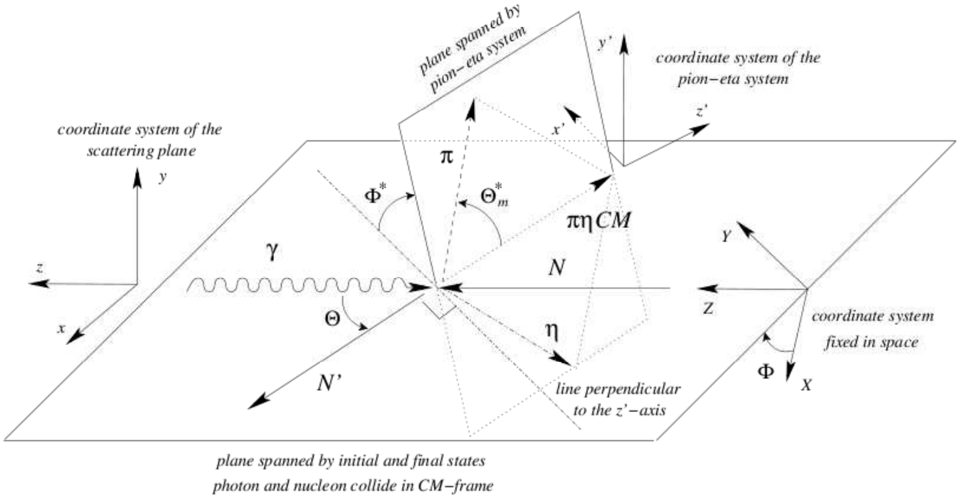

Figure 5.2: The coordinate system based on the scattering plane, which has its origin at the center of mass and contains the paths of the incident and scattered protons. Intersecting the scattering plane is a plane that contains the paths of the π^0 and η. The path of the scattered proton is along the line of intersection [21]

.

grated over all incoming photon energies. Figure 5.1(a) is from an earlier study, which was performed before the addition of the TAPS detector. The two large acceptance holes had to be extrapolated over during that analysis. Figure 5.1(b) is an equivalent plot for the current work, which indicates that this data covers the full angular range.

5.2 Five-Dimensional Acceptance Correction

In theory the acceptance may be a function of any of the parameters of the reaction. Each of the three particles in the final state has three degrees of freedom, giving a total of nine. However, there are also four constraint equations which effectively reduce the number of degrees of freedom. Consequently [21] the total number of degrees of freedom in the final state is:

$$D_f = N_p \cdot D_p - N_c = 3 \cdot 3 - 4 = 5 \tag{5.1}$$

where

N_p = number of particles in the final state

D_p = degrees of freedom per particle

N_c = number of constraint equations, i.e. conservation of mass, conservation of momentum, and the masses of the π^0 and η.

Consistent with this, a "five dimensional acceptance correction" is always required unless all angular distributions in all variables are flat:

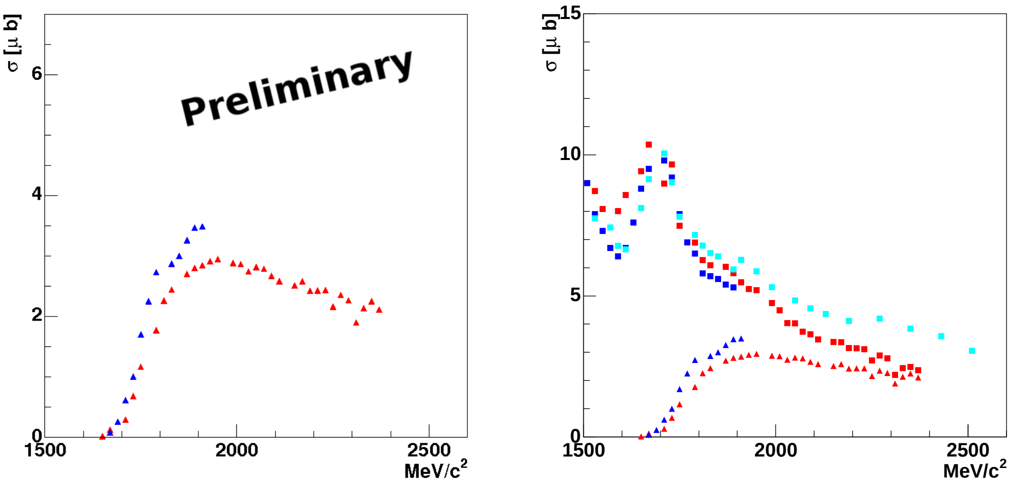

Figure 5.3: Total cross sections for the reactions $\gamma\mathrm{p} \rightarrow \mathrm{p}\pi^0\eta$ and $\gamma\mathrm{p} \rightarrow \mathrm{p}\pi^0\pi^0$. See text for details.

$$A_{i,j,k,l,m} = \frac{N_{MC,rec,i,j,k,l,m}}{N_{MC,gen,i,j,k,l,m}} , \tag{5.2}$$

where one such set of five parameters would be: i = energy bin for the incident photon, $j = \theta$, $k = \phi$, l = invariant mass of the $\mathrm{p}\pi^0$, and m = invariant mass of $\mathrm{p}\eta$.

Although a five dimensional acceptance correction is preferable, at this point we have based the acceptance criteria on only one dimension, which is the incident photon energy. All other variables have been integrated over, i.e. we have used only one bin for all remaining variables.

$$A_i = \frac{N_{rec,i}}{N_{gen,i}} \tag{5.3}$$

Figure 5.3 (left side) shows again the very preliminary total cross section for the reaction $\gamma\mathrm{p} \rightarrow \mathrm{p}\pi^0\eta$. The red triangles show our results, the blue triangles for comparison results from the GRAAL experiment. Though the shapes are consistent, a discrepancy is clearly observed. The right side of Fig. 5.3 shows in addition the very preliminary total cross section for the reaction $\gamma\mathrm{p} \rightarrow \mathrm{p}\pi^0\pi^0$. The red squares show our current CB-ELSA/TAPS results, the blue squares are from GRAAL and finally, the light blue squares show a previous CB-ELSA analysis. Discrepancies are also observed at higher energies.

At this point, the discrepancies remain unexplained. The earlier discussed missing five-dimensional acceptance correction could certainly be a reason. Moreover, the previous $\pi^0\eta$ and $\pi^0\pi^0$ analyses were based on data that did not cover the full angular range. For this reason, a model (partial wave analysis) was used to extrapolate over the acceptance holes. Any wrong assumption in the model could then lead to the observed deviations .

Chapter 6

Summary and Outlook

I have presented in this undergraduate thesis preliminary cross sections for the reaction $\gamma p \to \Delta\eta \to p\pi^0\eta$. My initial project included studies of the trigger thresholds and efficiencies for the data presented here. As a matter of fact, the trigger conditions were such that the same data set can be used to study different reactions. For this reason and to fully understand the efficiencies and acceptances of the experiment, we have compared a large variety of acceptance-corrected angular distributions from our data set to well-known differential cross sections from other reactions, e.g. single-meson reactions like $\gamma p \to p\pi^0$ and $\gamma p \to p\eta$. The agreement is very good to excellent showing our good understanding of the data. I was awarded a small travel grant of the NSF/DOE CEU program (Conference Experience for Undergraduate Students) and presented these results at the Fall '07 meeting of the Division of Nuclear Physics (division of the American Physical Society (APS)) at Jefferson Laboratory, Newport News, Virginia.

The η acts as an isospin filter and resonances decaying into $\Delta(1232)\eta$ must have isospin $I = 3/2$, i.e. must be Δ^* states themselves. For low photon energies, phase space is limited, and $\Delta(1232)$ and η should be in a relative S-wave. We can thus expect a high sensitivity for baryon resonances with isospin $I = 3/2$, spin $J = 3/2$, and negative parity. If such resonances decay into $N\pi$, they need $L = 2$ between N and π; resonances with these quantum numbers are characterized by $L_{2I,2J} = D_{33}$. The lowest mass resonance with these quantum numbers is $\Delta(1700)D_{33}$ and is assumed to couple strongly to $\Delta(1232)\eta$ (see also Fig. 1.1). This has been discussed in the literature [16].

The previous study on $\pi^0\eta$ photoproduction was completed in 2004 and reported by Igor Horn [22], before which the $\gamma p \to p\pi^0\eta$ cross section was unknown. That study included approximately 18,000 events, and was carried out at CB-ELSA before the addition of the TAPS detector. At this point, the collaboration was re-named to CB-ELSA/TAPS. The acceptance correction was applied by using weights for Monte-Carlo events based on the assumed amplitude in the partial wave analysis (PWA). The PWA suggests that the reaction proceeds via formation of five Δ^* resonances, $\Delta(1600)P_{33}$, $\Delta(1920)P_{33}$, $\Delta(1700)D_{33}$, $\Delta(1940)D_{33}$, $\Delta(1905)F_{35}$, and two N^* resonances $N(1880)P_{11}$ and $N(2200)P_{13}$.

A lot of work remains to be done to proceed with the current $\pi^0\eta$ analysis. An event-based PWA of our new data is in preparation to properly account for all correlations among the observables.

Bibliography

[1] N. F. Ramsey, Zeitschrift für Physik D Atoms, Molecules and Clusters **10**, 121 (1988).

[2] L. W. Alvarez and F. Bloch, Phys. Rev. **57**, 111 (1940).

[3] E. E. Chambers and R. Hofstadter, Phys. Rev. **103**, 1454 (1956).

[4] T. Frängsmyr, editor, *Nobel Lectures, Physics 1981-1999* (World Scientific Publishing, 1993).

[5] D. Griffiths, *Introduction to Elementary Particles* (John Wiley and Sons, 1987).

[6] S. Capstick and N. Isgur, Phys. Rev. **D34**, 2809 (1986).

[7] S. Capstick and W. Roberts, Prog. Part. Nucl. Phys. **45**, S241 (2000).

[8] Particle Data Group, W. M. Yao *et al.*, J. Phys. **G33**, 1 (2006).

[9] A. Das and T. Ferbel, *Introduction to Nuclear and Particle Physics* (World Scientific Publishing, 2003).

[10] R. Castelijns, *Photoproduction of strange mesons and hyperons on the proton*, PhD thesis, Rijksuniversiteit Groningen, 2006.

[11] W. Hillert, Eur. Phys. J. **A28S1**, 139 (2006).

[12] G. Suft *et al.*, Nucl. Instrum. Meth. **A538**, 416 (2005).

[13] E. Aker *et al.*, Nucl. Instrum. Meth. **A321**, 69 (1992).

[14] L. Hilger Crystals, Thallium doped CsI Data Sheet, 1999, `http://www.hilger-crystals.co.uk/prior/mat_csitl.htm`.

[15] A. R. Gabler *et al.*, Nucl. Instrum. Meth. **A346**, 168 (1994).

[16] I. Horn [CB-ELSA Collaboration], Eur. Phys. J. (2008), arXiv:0806.4251v1[nucl-ex], submitted.

[17] W. Verkerke and D. Kirkby, 2003, for documentation and source code, see `http://roofit.sourceforge.net`, arXiv:physics/0306116v1 [physics.data-an].

[18] R. Brun and F. Rademakers, Nucl. Instrum. Meth. **A389**, 81 (1997).

[19] `http://root.cern.ch`.

[20] W. Verkerke, Personal communication, 2008.

[21] A. Kiswandhi, *A Model for $\pi\pi$ and $\pi\eta$ Photoproduction*, PhD thesis, Florida State University, 2008.

[22] I. Horn, *The decay of the γp systen into the $p\pi^0\eta$ final state*, PhD thesis, Bonn University, 2004.